Thermal channelization of suprapermafrost flows

Katarzyna L.P. Warburton*[1], Joanmarie del Vecchio[2], Colin R. Meyer[3], and Marisa C. Palucis[4]

[1]Department of Applied Mathematics and Theoretical Physics, University of Cambridge, CB1 3AX, UK

[2]Department of Geology, College of William and Mary, Williamsburg, VA 23185, USA

[3]Thayer School of Engineering, Dartmouth College, Hanover, NH 03755 USA

[4]Department of Earth Sciences, Dartmouth College, Hanover, NH 03755 USA

February 18, 2025

- Feedback between flow and thaw of pore ice is proposed to explain water track formation and regular spacing
- Model predicts a dominant spacing of flow paths consistent with observations of water tracks at Toolik LTER station
- Further in-situ measurements of flow speed are needed to interpret future behavior of permafrost drainage networks

Abstract

On many frozen hillslopes, subsurface water above permafrost is routed through regularly spaced, linear features known as water tracks. We test whether water tracks form through thermal channelization, where heat from viscous dissipation in flowpaths deepens the active layer, creating a preferred flow path that attracts more water. We derive equations for suprapermafrost Darcy flow and, using linear stability analysis, we calculate growth rates and obtain wavelength selection for this system, which we compare to observed water track spacing from the high Arctic. Our model predictions are sensitive to flow speed, but the predicted cross-slope water track patterns are consistent with observed water track spacing under high flow conditions in the Low Arctic. Our model implies that signatures of changing climate might be found in changing water track spacing. However, feedback between flow and thaw is unlikely to drive flow path development in areas of low flow rate.

*klpw3@cam.ac.uk

Plain Language Summary

Water tracks move water across frozen landscapes, transferring water and nutrients from the uplands downstream to lakes and rivers, promote increased biological activity, and are an outsize source of greenhouse gasses. Sometimes these flow paths are equally spaced, and since other equally spaced flow paths associated with landscapes and ice seem to form from positive feedbacks between flow speed and melting or erosion, we tested whether this framework might explain water track appearance. We mathematically described the physics of the system and saw whether perturbations to that system grew or shrank depending on their size, and we found that the spacing (wavelength) of the resulting system matches well with observed spacing in nature if we chose a flow speed that is on the higher end of what has been observed in the field. These results imply that the physics we chose to represent this system are a good representation of the real world, but more field observations of these systems are needed.

1 Introduction

In cold regions, the presence of perennially frozen soil, or permafrost, modulates water infiltration and flow on soil-mantled slopes. On some frozen hillslopes in the Arctic and Antarctic, the impermeable permafrost table directs surface and subsurface flow paths into linear zones of enhanced soil moisture called water tracks (McNamara et al., 1999; Luoto, 2007; Levy et al., 2011; Tananaev, 2022; Trochim et al., 2016). These suprapermafrost flowpaths are theorized to result from the fact that peak discharge from spring snowmelt (Bring et al., 2016) coincides with a relatively shallow permafrost table, perching flowpaths at or near the surface (Hastings et al., 1989a; McNamara et al., 1999; Bring et al., 2016). Previous authors have noted the morphological similarity between water tracks in polar deserts and low-albedo streaks on other solar system bodies (Wray, 2021). However, many outstanding questions remain, including whether water tracks are transient or steady-state features of frozen landscapes, and whether the spacing or morphology of water tracks elucidates climate and/or topographic control on their formation (see reivew by Del Vecchio and Evans, 2025).

Across regional settings, water tracks have been observed to exhibit regular intertrack spacing, with track widths that scale with intertrack distance (Figure 1). In the High Canadian Arctic, 30 cm wide tracks are spaced about 1 m apart (Paquette et al., 2017); in the tundra of Alaska and Russia, tracks of 10-20 m width are spaced 20-60 m apart (Curasi et al., 2016; Tarbeeva et al., 2021; Del Vecchio et al., 2023). Antarctic water tracks generally do not exhibit regular spacing, though some isolated examples exist (Figure 1c) (Del Vecchio and Evans, 2025). The Arctic flowpaths are also often remarkably straight, and tend not to branch with adjacent flowpaths for kilometers (Fig 1a). Recurring slope lineae (RSL) on Mars also exhibit somewhat regular spacing (Fig. 1d). The formation of water tracks may thus be analogous to that of erosional rills (Smith and Bretherton, 1972) or dissolution karren (Bertagni and Camporeale, 2021), both of which have been described using linear stability analysis, a technique to model the onset of regularly spaced features. If thermal effects play a more important role, as sediment transport is rarely observed in water tracks (Del Vecchio and Evans, 2025), then better analogs that have also been studied via linear stability may be the channels that form by thaw on the tops of glaciers (Mantelli et al., 2015) or in the subglacial environment (Hewitt, 2011; Warburton et al., 2024).

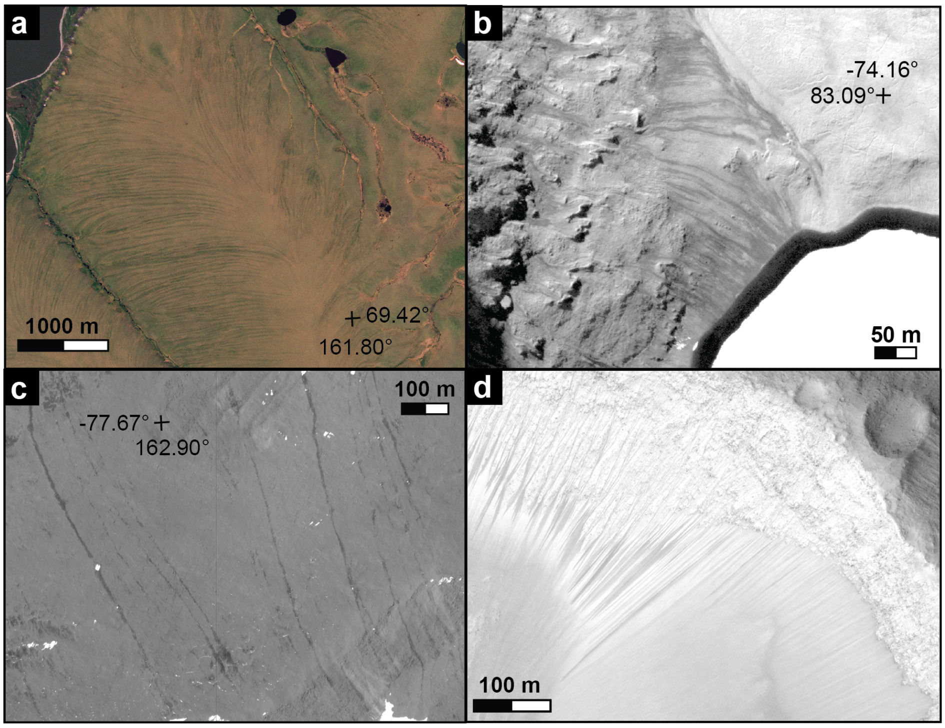

Figure 1: Four locations of flows exhibiting regular spacing in frozen landscapes.(a) Planet SuperDove true color image of Low Tundra vegetated water tracks in Russia near the Curasi et al. (2016) site. (b) Worldview2 panchromatic image of the Ward Hunt Island site described in Paquette et al. (2017). (c) WorldView2 panchromatic image of water tracks in the Taylor Valley, Antarctica (Levy et al., 2011). (d) RSL site in southeast Melas Chasma, Valles Marineris, Mars, visible in black and white HiRISE image ESP_031059_1685.

Water tracks comprise a large portion of the effective drainage network (McNamara et al., 1999), and their hypothesized position between saturation and incision thresholds may contribute to the pan-Arctic trend of low drainage densities in permafrost landscapes (Del Vecchio et al., 2024). Water tracks also play important biogeochemical roles in permafrost landscapes via the flux of water and nutrients from the uplands downstream to lakes and rivers (Evans et al., 2020). By promoting deeper thaw and flow of water and nutrients, water tracks promote increased biological activity (Harms et al., 2020; Cheng et al., 1998; Hastings et al., 1989b), resulting in water tracks being "hotspots" of greenhouse gasses relative to their surface area on landscapes (Harms et al., 2020). Discovering the environmental factors that set water track spacing is important because changing climate conditions may promote disturbance in water tracks on a landscape experiencing perturbations (i.e. climate change) that would drive a change in track configuration (Del Vecchio et al., 2024; Evans et al., 2022).

Although previous authors have speculated on site-specific factors leading to flowpath initiation and form, no unified theory of water track initiation and spacing exists (Tananaev, 2022; Del Vecchio and Evans, 2025). Some hypothesize they work like erosional rills, but do not develop into true fluvial channels due to high incision thresholds imparted by frozen ground and/or the eluviation of fines and the leaving of a coarse lag (McNamara et al., 1999; Paquette et al., 2017; Del Vecchio et al., 2023). In this model the balance of fluvial incision (advection) and soil movement via creep-like processes (diffusion) would operate as in temperate landscapes (e.g. Smith and Bretherton, 1972; Izumi and Parker, 1995; Smith, 2010) with the caveat of seasonally imparted erosion thresholds. Other authors suggest water tracks are merely the saturated surface expression of degrading ice wedge polygons and other (thermally controlled) patterned ground such as "nonsorted stripes" (Paquette et al., 2017; Tarbeeva et al., 2021; Tananaev, 2022). Harris et al. (2025) suggest that water flow is a side effect, rather than a driver, of water track patterns, and water track spacing is associated with pre-existing patterned ground. Parr et al. (2020) suggest windblown snow preferentially forms protective drifts in upwind water tracks, enhancing spring runoff and erosion, while downwind tracks remain exposed, leading to evolution of the observed spacing; however, these authors did not propose that this mechanism initiates water tracks. We hypothesize here that an important mechanism for water track initiation is the generation of heat via flow in water tracks, driving focused thaw and initiating a positive feedback, by analogy with supra- and sub-glacial channels (Mantelli et al., 2015; Hewitt, 2011; Warburton et al., 2024)..

In this paper we develop a model for heat transport in a suprapermafrost hillslope environment, accounting for the heat produced by viscous dissipation in the flowing water warming the surrounding cold soil. We perform a linear stability analysis of the model, to calculate the rate at which periodically spaced perturbations, i.e. localized thaw of the permafrost table, grow from a laterally uniform background state, as a function of the wavelength between features. Positive growth rates are indicative of the potential for instability (i.e. water track development), and the wavelength with the largest growth rate may correspond to the spacing of the eventual water tracks. We show that the most unstable wavelength is consistent with the spacing of water tracks on the North Slope of Alaska when field-measured temperature profiles and upper estimates of flow conditions are used. We discuss implications of assuming this thermal mechanism for water track formation to predict changes in water routing under warming conditions, while also considering alternative mechanisms for water track development in regions where this thermal model does not indicate a channelizing instability.

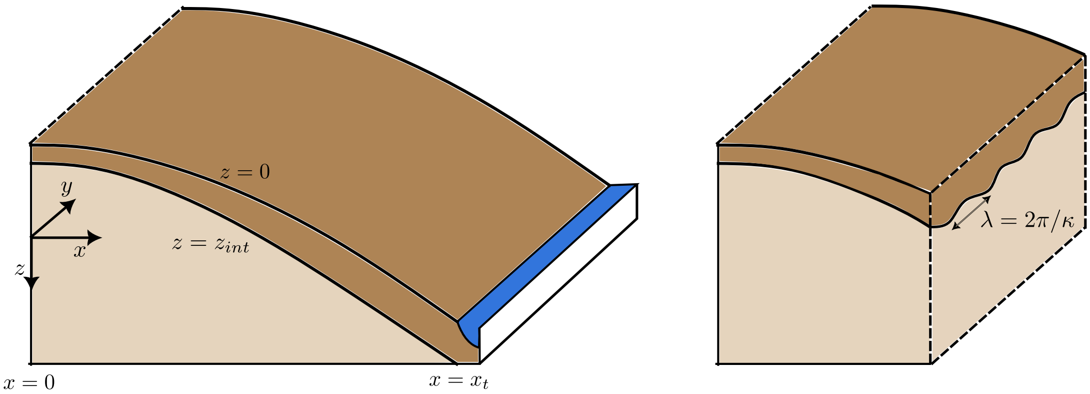

Figure 2: (a) A diagram of the suprapermafrost landscape, showing the hillslope from $x = 0$ to the stream at $x = x_t$. The ground is frozen below $z = z_{int}$, measured from the surface at $z = 0$. (b) Cross-section showing the development of periodic fluctuations in thaw depth orthogonal to the flow direction.

2 Model for water track initiation

In this section, we develop a model of flow and thermal evolution designed to represent hillslopes in the vegetated Low Arctic. We consider water track evolution along a parabolic hillslope (Gilbert, 1909) which starts at a flat summit at $x = 0$ and ends at a stream at its toe, $x = x_t$. Our soil consists of an unfrozen layer, from $z = 0$ to $z = -z_{int}$, on top of a frozen layer, from $z = -z_{int}$ downwards (figure 2). We assume the unfrozen layer is fully water-saturated and the frozen layer is fully ice-saturated. Our aim is to track the thaw of ice from the pore space, leading to migration of this top of the permafrost table, z_{int}, in time and space, accounting for the heat produced by the flow of water.

2.1 Flow model

We assume that water flows through the unfrozen layer according to Darcy's law,

$$\boldsymbol{u} = -\frac{k_0}{\mu}(\nabla p - \rho_w g \hat{z}), \tag{1}$$

where $\boldsymbol{u}$ is the Darcy flux, k_0 is an effective permeability for the unfrozen layer, μ is the viscosity of water, ρ_w is the density of water, g is gravity, and p is the water pressure. The stream at x_t acts as a sink, with a fixed pressure head $p(x_t) = p_t$. Due to the aspect ratio of the flow, with water tracks much shallower than the horizontal scale of variations, we ignore the vertical component of $\boldsymbol{u}$ and consider only flow that is parallel to the surface of the hillslope, meaning that pressure is hydrostatic.

Assuming that the whole of the unfrozen layer is saturated, the water flux through the unfrozen layer is, by integration of the Darcy flux, $\boldsymbol{q} = z_{int}\boldsymbol{u}$. We assume there is no flow in the frozen layer. Thus, conservation of mass is given by

$$\boldsymbol{\nabla} \cdot \boldsymbol{q} = 0, \tag{2}$$

assuming that the water level equilibrates fast compared to the timescale of permafrost thaw, and that all water joins the flow from rain or snow melt at the top of the hillslope.

2.2 Thermal model

We assume the temperature within the unfrozen and frozen layers obeys the heat equation, with thermal conductivities k_u and k_f, and specific heat capacities C_u and C_f, respectively. Given that the flow is predominantly downslope, while the temperature gradients are expected to be primarily vertical (and lateral between track and intertrack), we neglect advection of heat by the flow as compared to diffusion.

Thus the temperature within the unfrozen region is governed by

$$C_u \rho_u \frac{\partial T_u}{\partial t} = k_u \nabla^2 T_u + Q, \tag{3}$$

where dissipation within the water flow provides an internal heat source of

$$Q = |\boldsymbol{u} \cdot \nabla p| = \frac{k_0}{\mu} |\boldsymbol{\nabla} p|^2, \tag{4}$$

while within the frozen region, there is no flow and therefore no internal heat source, and the heat transfer is represented by

$$C_f \rho_f \frac{\partial T_f}{\partial t} = k_f \nabla^2 T_f. \tag{5}$$

The interface between the layers, z_{int}, is by definition at freezing point, $T_u(-z_{int}) = T_f(-z_{int}) = T_m$, while a balance of latent and sensible heat fluxes across the interface means that the melt-rate is given by

$$\rho_w \phi L \frac{\partial z_{int}}{\partial t} = k_u \frac{\partial T_u}{\partial z} - k_f \frac{\partial T_f}{\partial z}, \tag{6}$$

where L is the latent heat of fusion, ϕ is the pore fraction occupied by water/ice, and ρ_w is the density of water that is changing phase.

At the surface, we apply a heat flux coming from a combination of incoming solar radiation, F_{rad}, assumed constant in space, and a conductive heat flux proportional to the difference between the soil surface temperature, $T_u(0)$, and the air temperature, T_a, giving

$$k_u \left. \frac{\partial T_u}{\partial z} \right|_{z=0} = F_{rad} + \beta[T_a - T_u(0)]. \tag{7}$$

The parameter β describes the insulation provided by a thermal boundary layer at the surface, e.g. within a snow or vegetation layer, to account for the observed difference between air and soil temperature.

2.3 Linear stability analysis

We write the depth of the frozen-interface as

$$z_{int} = \bar{z}_{int}(x,t) + \hat{z}_{int}(x) e^{i\kappa y + \sigma t}, \tag{8}$$

where $\bar{z}_{int}$ is the laterally averaged value, and $\hat{z}_{int}$ is the amplitude of the perturbation at a wavelength $\lambda = 2\pi/\kappa$, which has growth rate $\sigma(\kappa)$. We linearize the governing equations to write the perturbations to all other quantities in terms of $\hat{z}_{int}$, then solve for $\sigma(\kappa)$ in terms of key landscape variables (topography, ϕ, β, $\partial T_f/\partial z$).

Details of the calculation are given in the Supplementary Information. We find that the shortest wavelengths are stabilized by diffusion of heat through the frozen layer away from the water tracks, while the longest wavelengths are stable because the fixed total water availability on the hillslope discourages the formation of very large flow-paths, which are hard to fill. Intermediate wavelengths are unstable due to the additional heating provided by a greater depth of flow.

The fastest-growing wavelength of instability, $\lambda = 2\pi/\kappa$, is given by

$$\frac{\kappa^{8/3}}{\sqrt{\kappa^2 + C_f\rho_f\left(\bar{Q} - \beta\frac{\partial \bar{T}_u}{\partial z}\right)/k_f\rho_w\phi L}} = \frac{2.0374\,\bar{Q}}{k_f\frac{\partial \bar{T}_f}{\partial z}x_t^{2/3}} \tag{9}$$

which has growth rate

$$\sigma_{max} \approx \frac{1}{\rho_w\phi L}\left(\bar{Q}(x_t) - \beta\left.\frac{\partial \bar{T}_u}{\partial z}\right|_{-\bar{z}_{int}}\right), \tag{10}$$

where

$$\bar{Q} = \bar{u}\frac{d\bar{p}}{dx} = \bar{u}\rho_w g\sin\theta \tag{11}$$

is the maximum heat dissipation by water flow, the product of flow speed $\bar{u}$ and the down-slope hydrostatic pressure gradient at the toe of the hillslope for a slope angle θ. Figure 3 shows values of the fastest-growing wavelength and associated growth rate for the parameter values determined in the next section.

3 Parameter constraints from Low Arctic data

Our model predicts that water track spacing is sensitive to the topographic parameters of hillslope length and slope, the soil properties of porosity, thermal conductivity and specific heat capacity, the water flow speed, the depth of thaw, and temperature gradients at the top of the permafrost table. The spacing also depends on well-constrained physical constants such as the latent heat of freezing, detailed in Table S2.

Our model most closely resembles water tracks described in the vegetated Low Arctic, as opposed to those in the High Canadian Arctic (where the flowpaths are not parallel; Paquette et al., 2017) or Antarctica (where the soil is not fully saturated; Levy et al., 2011). We extract topographic data from remote sensing in locations with water tracks from across the Low Arctic (Evans et al., 2020; Rushlow et al., 2020). However, due to limited in-situ data availability, we focus mainly on the Toolik Lake Long-Term Ecological Research (LTER) station, hereafter "Toolik", for which we analyzed air temperature, temperature probe data, and discharge data collected from various water track locations (Godsey, 2020a,b; Evans et al., 2020). Figure 3 illustrates that while our model can be applied to the varied topography of the Low Arctic, and the results do depend on e.g. hillslope angle, our predictions are sensitive to the in-situ data, a feature we discuss further in Section 4.2.

3.1 Topographic data

We collected seven topographic profiles of convex soil-mantled hillslopes bearing water tracks to assess realistic topographic inputs (maximum angle, length of slope, shape of profile) to the model. We used the 2 m ArcticDEM elevation product (Porter et al., 2022) as hosted on Google Earth Engine; two profiles were drawn in Alaska, one in Yukon, one in Nunavut, and three in Siberia, constituting a representative sampling of locations in which we have observed water tracks on parabolic hillslopes, shown in Supplementary Figure S3.

3.2 Flow rate data

Using published data on discharge of water tracks at Toolik (Evans et al., 2020), we define a range of observed water track flow rates by discharge and approximated water track cross-sectional area during high flows with minimal thaw depths in June and average flows with maximum thaw depths in August, producing flow rates of $\sim 10^{-4}$ and 10^{-2} m/s, respectively (Godsey (2020c); Evans et al. (2020); Table S4). We also recorded video footage of vegetation being transported by flow following a rain event (Movie S1). Particle tracking of this video suggests a higher flow speed of around 0.25 m/s at that time.

3.3 Thermal data

We used publicly available data from Toolik (Godsey, 2020a,b) to extract soil temperature gradients in the frozen and unfrozen layers of soil, a key control on predicted wavelengths and growth rates. We calculated temperature profiles at Water Track 6 at Toolik with depth in 10-day averages over the data collection period to derive the depth of thaw and thermal gradients throughout the profile. For evaluating the model, we extracted typical thaw depths $\bar{z}_{int}$ from June to August, and the range of thermal gradients $\partial\bar{T}/\partial z$ observed just above and just below the permafrost table over this time frame.

The thermal properties of the soil depend on the porosity ϕ. We chose a porosity of 0.9, consistent with numerical models of water tracks (Evans et al., 2020), to calculate bulk thermal properties of frozen and unfrozen soil whose void spaces are filled with ice and water, respectively (Wang et al., 2020).

As an estimate of conductive vs radiative heat flux, we assumed insulation from a snow depth of 0.5 m, which is typical for May/June (Rushlow et al., 2020) with an additional 0.2 m of tundra vegetation mat. Conduction through 0.7 m of air gives and an indeed small value of $\beta \approx 0.026 \mathrm{W\,m^{-1}\,K^{-1}}/0.7\mathrm{m} = 0.04 \mathrm{W\,m^{-2}\,K^{-1}}$.

4 Results and discussion

Our model of thermal channelization predicts that the fastest-growing wavelength should be given by equation (9). Evaluating this expression using estimated parameters at Toolik (Table S4), we find a range of wavelengths, inversely proportional to the water flow speed. As noted in section 3.2, there is considerable uncertainty in the flow speed, leading to a range of predicted wavelengths (figure 3). The corresponding growth rates (equation 10) are shown in figure 3b.

4.1 Model results versus field observations

At Toolik, the maximum hillslope angle is $\theta = 4.8°$, and the hillslope length is $x_t = 1600$ m. As shown in figure 3c,d at the lower end of observed flow speeds, our model predicts

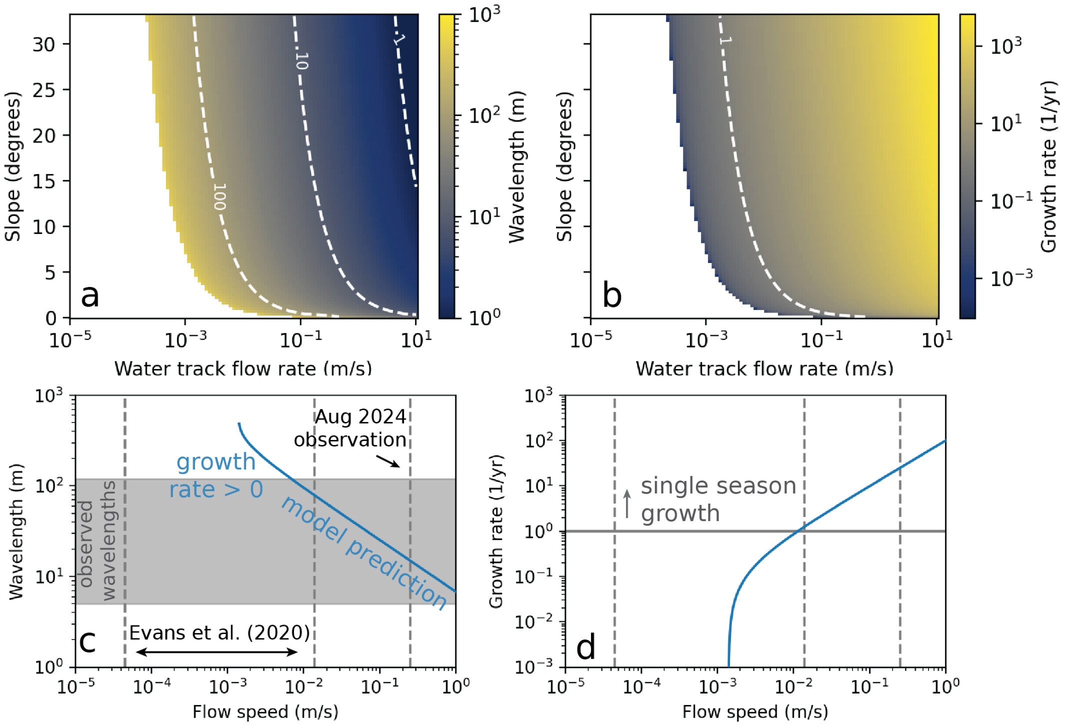

Figure 3: Model results compared to field observations (a) Contours of fastest growing unstable wavelength for a range of hillslope angles and water track flow rates, calculated from equation (9). All other parameter values correspond to Toolik (Table S4). Dashed lines demonstrate the approximate range and average water track spacing observed around the Arctic and Antarctic (range: 1-100 m). Wavelengths are not given where the system is predicted to be stable. (b) Corresponding growth rates from equation (10). Negative growth rates (stable system) are shown in white. (c) Predicted wavelength (blue line) at hillslope angle corresponding to Toolik, as a function of flow speed. Dashed lines indicate the range speeds inferred from Godsey (2020c) (Table S4) and the August 2024 field observation. Horizontal bar shows range of flowpath spacing observed from satellite imagery at the WT6 site.(d) Corresponding predicted growth rate, for the same conditions as (c). Horizontal bar denotes regime where growth rate exceeds 1/year, indicating flow speeds must be above 10^{-2} m s^{-1} for an instability to develop over a single season.

that thermal channelization should not take place. The predicted wavelengths are an order of magnitude too large (figure 3c), and the growth rates are either negative, or below 1/yr, indicating that Darcy flow at this speed would not generate enough heat to lead to thaw a significant channel feature over the course of a season.

However, at higher observed flow rates, corresponding to the conditions after a rain event, the predicted wavelengths are within the 5-120 m range of observed water track spacings at Toolik. Further, the associated growth rates reach 10^2/yr, large enough that a thermal flow-thaw feedback mechanism could plausibly lead to the initiation of the observed patterning in the wake of rain or snowmelt events. Further in-situ and flume-based flow measurements would add confidence in the model results, particularly in better understanding the flow and permeability structure.

4.2 Controls on water track spacing assuming a thermal mechanism

Across a range of realistic field parameters, we predict that water track spacing is inversely proportional to flow rate and slope (Figures 3, S1). The spacing increases slightly with hillslope length and strength of the temperature gradient in the permafrost (Figure S1). The growth rate is most sensitive to flow rate, slope, insulation between air and water temperature, and the temperature gradient in the permafrost. Paralleling the proposed "top-down" climate and "bottom-up" geology controls on water track properties (Del Vecchio and Evans, 2025), we can also consider how these factors might influence water track initiation and spacing. In our model the climate factors include temperature gradients as well as water availability (flow rate) as well as snow and/or tundra vegetation thickness (controls on insulation). Geologic and geomorphic factors include hillslope length and angle and soil porosity/hydraulic conductivity (which is also modulated by tundra vegetation). We might therefore expect to see trends in water track spacing and occurrence with rain fall, slope angle and, to a lesser extent, hillslope length.

Climatic factors may change as amplified Arctic warming progresses, shifting both temperatures and hydroclimates. Warming of the Arctic (Masson-Delmotte et al., 2019; Rantanen et al., 2022) will likely shift the depth of the active layer and thermal gradients in the permafrost below. In the Arctic, it is also predicted that less precipitation may fall as snow and more precipitation may fall as rain (Bintanja and Andry, 2017; Landrum and Holland, 2020) with increased extreme rainfall events (Tebaldi et al., 2006). Within our flow-heating model of water track initiation, the spatial density of water tracks is predicted to increase strongly with rainfall.

In fact, we observed what appears to be at least one incipient water track forming between existing water tracks spaced about 80 meters apart near the Toolik LTER (Figure 4). Differencing DEMs created from lidar scans in 2017 and 2022 showed a slope-perpendicular, streak-like pattern of subsidence that resembles the morphology of the nearby tracks. When visiting this feature in August 2024, we noted thermokarst-like disturbance of the tundra, taller and greener grasses (Figure S4), and enhanced moisture in this area, implying a water track is forming. This dynamic could be evidence for climate control on water track spacing. As climate changes, the thermal and hydrologic state of the hillslope changes, and so might the most unstable wavelength. In this case, higher flow speeds might be driving the formation of more closely spaced water tracks.

Interestingly, water track spacing in the Low Arctic is quite consistent, on the scale of 10s of m, and frequently between 20-60 m (Del Vecchio and Evans, 2025; Tananaev, 2022), a pattern occasionally observed in other polar settings (Figure 1), which may appear to conflict with the predicted dependence on topography. However, sensitivity analysis (figure S1a) shows that our model consistently predicts that, independent of hillslope shape, whenever the growth rate exceeds 1/year (i.e. single season formation), the fastest growing mode remains below 100 m, although this is sensitive to the values taken for surface insulation and thermal gradient. While encouraging that our model captures the range of spacings at the Toolik site given site-specific parameters, the limited variability in spacing across the Arctic serves as a reminder that the parameters of our model may be inter-correlated, such that predicting large-scale regional trends requires further in-situ measurements, particularly of flow rate and thermal state.

4.3 Model limitations and extensions

As a novel exploration of the initiation of water tracks using linear stability analysis, we make certain simplifying assumptions based on the setting and data availability which may not apply across polar settings in general. These could be relaxed in future work, especially if supported by field observations or flume data. We assume a permeability that is constant in time and space. However, permeability may evolve in time due to erosion or sediment transport associated with flow in the water track. Thus, we may be underestimating the growth rate of flow-driven instabilities by neglecting this possible feedback mechanism. Conversely, assuming that permeability is constant with depth may lead to an overestimate of the growth rate, by overestimating the flow speed close to the frozen-thawed interface.

Our thermal feedback mechanism does not predict water track characteristics in the High Canadian Arctic and in Antarctica, and there is field evidence that our mechanism is not applicable in these settings. In the High Canadian Arctic, the water flowing through preferential flowpaths has a cooling effect on the soil and leads to shallower thaw under these flowpaths, an anomalous occurrence in the literature (Paquette et al., 2017; Del Vecchio and Evans, 2025). In the Antarctic, there is often no regular spacing and conditions are far from saturated; flowpaths are also not found on convex hillslopes. In these two non-vegetated landscapes, the association of water tracks with ice wedges, polygons, and “non-sorted stripes” has been noted (Del Vecchio and Evans, 2025). Recent work using ground-penetrating radar determined that in the Low Arctic, under the tundra, water tracks were also forming associated with ice wedges, which were otherwise invisible at the surface (Harris et al., 2025). Thus, a potential alternative mechanism may involve linking water tracks to massive subsurface ice. Our model also does not predict the close spacing (<10 m) of RSL on Mars (Figure 1d), where any liquid flow rates are likely low (Huber et al., 2020), implying the thermal feedback mechanism may not operate in that system either.

We note that our model is fundamentally a linear model for feature initiation. However, observations of water tracks show them to be a persistent, non-linear feature of the landscape. The spacing of water tracks may not conform to the spacing of the linear instability (c.f. subglacial channels, Warburton et al., 2024), but instead reflect non-linear interactions that develop in the wake of pattern initiation. The initial patterning may be due to thaw-flow feedbacks as explored in this work, or another source of heterogeneity in the landscape, or both. Future work could explore the non-linear flow and temperature patterns that develop around an established water track.

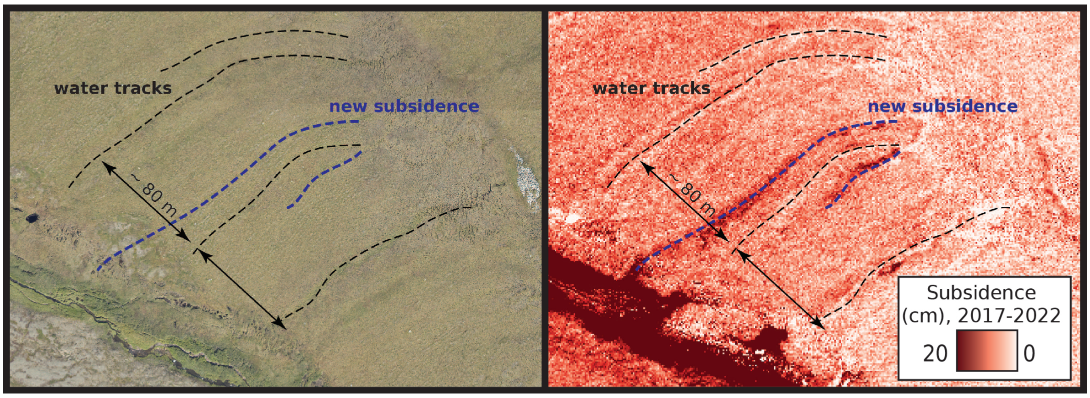

Figure 4: Potential initiation of a new water track around Toolik Lake observed in remote sensing. (a) True-color image of hillslide with existing water tracks and location of subsidence observed in lidar. (b) DEM of difference from 2017 to 2022 lidar surveys demonstrating linear zones of subsidence. Field photo of this location can be found in Figure S4.

5 Conclusions

We developed a model to describe and test the hypothesis that suprapermafrost flowpaths (water tracks) develop from a feedback between porous media flow and thaw of the pore space ice. By employing linear stability analysis, we extracted the fastest growing wavelengths of instability in the system and compared them to the observed separation between water tracks in the vegetated Low Arctic. Our model does successfully replicate observed inter-track distances using conditions at Toolik Lake Long-Term Ecological Research station. We suggest that water track density may increase in response to increasing rain events, although not necessarily across the whole Arctic.

Open Research Section

Data for air temperature, soil temperature, and discharge at water tracks are derived from Godsey (2020a, 2020b, 2020c). Digital elevation models derived from lidar collected by NEON (National Ecological Observatory Network) can be found at National Ecological Observatory Network (NEON) (2025a,b). High-resolution imagery for the Toolik area collected by NEON can be found at National Ecological Observatory Network (NEON) (2025c,d). Code to generate the figures (including collecting topographic data) is available at DelVecchio (2025).

KW is supported by a Junior Research Fellowship (Trinity College, Cambridge). JD, CM, and MP are supported by NSF grant 2311319. Fieldwork to the Toolik Lake LTER was supported by startup funds at William and Mary. We thank Joe Levy and Shawn Chartrand of discussions on Antarctic and High Canadian Arctic water tracks, respectively. We thank Sarah Evans and Sarah Godsey for their data collection, field support, and discussions. We acknowledge that Toolik Field Station and the surrounding areas are located on the ancestral hunting grounds of the Nunamiut, and occasional hunting grounds and routes of the Gwich'in, Koyukuk, and Iñupiaq peoples. Toolik Field Station and its inhabitants recognize, and are grateful for, the Indigenous people who inhabit and steward the land.

References

Bertagni, M. and Camporeale, C. (2021). The hydrodynamic genesis of linear karren patterns. *Journal of Fluid Mechanics*, 913:A34.

Bintanja, R. and Andry, O. (2017). Towards a rain-dominated arctic. *Nature Climate Change*, 7(4):263–267.

Bring, A., Fedorova, I., Dibike, Y., Hinzman, L., Mård, J., Mernild, S. H., Prowse, T., Semenova, O., Stuefer, S. L., and Woo, M. K. (2016). Arctic terrestrial hydrology: A synthesis of processes, regional effects, and research challenges. *Journal of Geophysical Research G: Biogeosciences*, 121(3):621–649.

Cheng, W., Virginia, R., Oberbauer, S. F., Gillespie, C. T., Reynolds, J. F., and Tenhunen, J. (1998). Soil nitrogen, microbial biomass, and respiration along an arctic toposequence. *Soil Science Society of America Journal*, 62(3):654–662.

Curasi, S. R., Loranty, M. M., and Natali, S. M. (2016). Water track distribution and effects on carbon dioxide flux in an eastern siberian upland tundra landscape. *Environmental Research Letters*, 11(4):045002. Publisher: IOP Publishing.

Del Vecchio, J. and Evans, S. G. (2025). Climate and hydrogeological controls on water tracks in permafrost landscapes. *Reviews of Geophysics*.

Del Vecchio, J., Palucis, M. C., and Meyer, C. R. (2024). Permafrost extent sets drainage density in the arctic. *Proceedings of the National Academy of Sciences*, 121(6):e2307072120.

Del Vecchio, J., Zwieback, S., Rowland, J. C., DiBiase, R. A., and Palucis, M. C. (2023). Hillslope-channel transitions and the role of water tracks in a changing permafrost landscape. *Journal of Geophysical Research: Earth Surface*, 128(9):e2023JF007156.

DelVecchio, J. (2025). jmdelvecchio/wt-lin-stability: v0.1. https://doi.org/10.5281/zenodo.14826280 [Software].

Evans, S. G., Godsey, S., Chew, C., Yokeley, B., Hatch, K., Ferm, E., Harris, R. H., Crosby, B. T., Gooseff, M. N., Mohammed, A. A., et al. (2022). Saturation dynamics along thawing continuous permafrost hillslopes. In *AGU Fall Meeting Abstracts*, volume 2022, pages EP36B–03.

Evans, S. G., Godsey, S. E., Rushlow, C. R., and Voss, C. (2020). Water tracks enhance water flow above permafrost in upland arctic alaska hillslopes. *Journal of Geophysical Research: Earth Surface*, 125(2).

Gilbert, G. K. (1909). The convexity of hilltops. *The Journal of Geology*, 17(4):344–350.

Godsey, S. (2020a). Air temperature at water track site wt6. Arctic Data Center. https://arcticdata.io/catalog/view/15f8ac93-37f2-4045-b45b-35d078b82b46.

Godsey, S. (2020b). Soil temperatures at water track sites. Arctic Data Center. https://arcticdata.io/catalog/view/8fa6477d-f846-4daa-b053-c799a8b11825.

Godsey, S. (2020c). Synoptic discharge at water track sites. Arctic Data Center. https://arcticdata.io/catalog/view/0e6561e3-33bf-46d6-aba4-745be63c0e19.

Harms, T. K., Rocher-Ros, G., and Godsey, S. E. (2020). Emission of greenhouse gases from water tracks draining arctic hillslopes. *Journal of Geophysical Research: Biogeosciences*, 125(12):e2020JG005889.

Harris, R. H., Evans, S. G., Marshall, S. T., Godsey, S. E., and Parsekian, A. D. (2025). Using ground-penetrating radar to infer ice wedge characteristics proximal to water tracks. *Journal of Geophysical Research: Earth Surface*, 130(1):e2024JF007832.

Hastings, S. J., Luchessa, S. A., Oechel, W. C., and Tenhunen, J. D. (1989a). Standing biomass and production in water drainages of the foothills of the philip smith mountains, alaska. *Ecography*, 12(3):304–311. _eprint: https://onlinelibrary.wiley.com/doi/pdf/10.1111/j.1600-0587.1989.tb00850.x.

Hastings, S. J., Luchessa, S. A., Oechel, W. C., and Tenhunen, J. D. (1989b). Standing biomass and production in water drainages of the foothills of the philip smith mountains, alaska. *Ecography*, 12(3):304–311.

Hewitt, I. J. (2011). Modelling distributed and channelized subglacial drainage: the spacing of channels. *Journal of Glaciology*, 57(202):302–314.

Huber, C., Ojha, L., Lark, L., and Head, J. W. (2020). Physical models and predictions for recurring slope lineae formed by wet and dry processes. *Icarus*, 335:113385.

Izumi, N. and Parker, G. (1995). Inception of Channelization and Drainage Basin Formation: Upstream-Driven Theory. *Journal of Fluid Mechanics*, 283(April 2014):341–363. ISBN: 0022112095002.

Landrum, L. and Holland, M. M. (2020). Extremes become routine in an emerging new arctic. *Nature Climate Change*, 10(12):1108–1115.

Levy, J. S., Fountain, A. G., Gooseff, M. N., Welch, K. A., and Lyons, W. B. (2011). Water tracks and permafrost in taylor valley, antarctica: Extensive and shallow groundwater connectivity in a cold desert ecosystem. *Bulletin of the Geological Society of America*, 123(11):2295–2311.

Luoto, M. (2007). New insights into factors controlling drainage density in subarctic landscapes. *Arctic, Anarctic and Alpine Research*, 39(1):117–126.

Mantelli, E., Camporeale, C., and Ridolfi, L. (2015). Supraglacial channel inception: Modeling and processes. *Water Resources Research*, 51:7044–7063.

Masson-Delmotte, V., Zhai, P., Pörtner, H.-O., Roberts, D., Skea, J., Shukla, P. R., Pirani, A., Moufouma-Okia, W., Péan, C., Pidcock, R., et al. (2019). Global warming of 1.5 c. *An IPCC Special Report on the impacts of global warming of*, 1:93–174.

McNamara, J. P., Kane, D. L., and Hinzman, L. D. (1999). An analysis of an arctic channel network using a digital elevation model. *Geomorphology*, 29:339–353.

National Ecological Observatory Network (NEON) (2025a). Elevation - lidar (dp3.30024.001).

National Ecological Observatory Network (NEON) (2025b). Elevation - lidar (dp3.30024.001).

National Ecological Observatory Network (NEON) (2025c). High-resolution orthorectified camera imagery mosaic (dp3.30010.001).

National Ecological Observatory Network (NEON) (2025d). High-resolution orthorectified camera imagery mosaic (dp3.30010.001).

Paquette, M., Fortier, D., and Vincent, W. F. (2017). Water tracks in the high arctic: a hydrological network dominated by rapid subsurface flow through patterned ground. *Arctic Science*, 3(2):334–353.

Parr, C., Sturm, M., and Larsen, C. (2020). Snowdrift landscape patterns: An arctic investigation. *Water Resources Research*, 56(12):e2020WR027823.

Porter, C., Howat, I., Noh, M.-J., Husby, E., Khuvis, S., Danish, E., Tomko, K., Gardiner, J., Negrete, A., Yadav, B., Klassen, J., Kelleher, C., Cloutier, M., Bakker, J., Enos, J., Arnold, G., Bauer, G., and Morin, P. (2022). ArcticDEM - Strips, Version 4.1.

Rantanen, M., Karpechko, A. Y., Lipponen, A., Nordling, K., Hyvärinen, O., Ruosteenoja, K., Vihma, T., and Laaksonen, A. (2022). The arctic has warmed nearly four times faster than the globe since 1979. *Communications earth & environment*, 3(1):168.

Rushlow, C. R., Sawyer, A. H., Voss, C. I., and Godsey, S. E. (2020). The influence of snow cover, air temperature, and groundwater flow on the active-layer thermal regime of arctic hillslopes drained by water tracks. *Hydrogeology Journal*, 28(6):2057–2069.

Smith, T. R. (2010). A theory for the emergence of channelized drainage. *Journal of Geophysical Research: Earth Surface*, 115(F2). _eprint: https://agupubs.onlinelibrary.wiley.com/doi/pdf/10.1029/2008JF001114.

Smith, T. R. and Bretherton, F. P. (1972). Stability and the conservation of mass in drainage basin evolution. *Water Resources Research*, 8(6):1506–1529. _eprint: https://agupubs.onlinelibrary.wiley.com/doi/pdf/10.1029/WR008i006p01506.

Tananaev, N. (2022). Defrosting northern catchments: Fluvial effects of permafrost degradation. *Earth-Science Reviews*, 228:20.

Tarbeeva, A. M., Tregubov, O. D., and Lebedeva, L. S. (2021). Structure of the slope trough network of the cryolithozone in the vicinity of Anadyr. *Geomorfologiya*, 52(1):109–120. Number: 1.

Tebaldi, C., Hayhoe, K., Arblaster, J. M., and Meehl, G. A. (2006). Going to the extremes: an intercomparison of model-simulated historical and future changes in extreme events. *Climatic change*, 79:185–211.

Trochim, E. D., Jorgenson, M. T., Prakash, A., and Kane, D. L. (2016). Geomorphic and biophysical factors affecting water tracks in northern alaska. *Earth and Space Science*, pages 123–141.

Wang, K., Jafarov, E., and Overeem, I. (2020). Sensitivity evaluation of the kudryavtsev permafrost model. *Science of the Total Environment*, 720:137538.

Warburton, K. L. P., Meyer, C. R., and Sommers, A. N. (2024). Predicting the onset of subglacial drainage channels. *Journal of Geophysical Research: Earth Surface*, 129(12):e2024JF007758. e2024JF007758 2024JF007758.

Wray, J. J. (2021). Contemporary liquid water on mars? *Annual Review of Earth and Planetary Sciences*, 49(1):141–171. _eprint: https://doi.org/10.1146/annurev-earth-072420-071823.

Supplement: "Thermal channelization of suprapermafrost flows"

Katarzyna L.P. Warburton*[1], Joanmarie del Vecchio[2], Colin R. Meyer[3], and Marisa C. Palucis[4]

[1]Department of Applied Mathematics and Theoretical Physics, University of Cambridge, CB1 3AX, UK
[2]Department of Geology, College of William and Mary, Williamsburg, VA 23185, USA
[3]Thayer School of Engineering, Dartmouth College, Hanover, NH 03755 USA
[4]Department of Earth Sciences, Dartmouth College, Hanover, NH 03755 USA

February 18, 2025

Contents of this file

Introduction

In this supplemental document, we include full details of the linear stability analysis calculation, additional sensitivity analysis and field data plots, a table of variables and parameters and their values, and a caption for the supplementary video.

Text S1 Linear stability analysis

In our analysis, we allow our background state (which we denote with overbars) to vary along the length of the hillslope but to have no cross-slope variation; i.e. $\bar{T}_u(x, z, t)$ denotes the average temperature profile at along-slope position x and depth z, at time t. The inclusion of time in the background state is to account for the yearly freeze-thaw cycles that occur in permafrost landscapes. Rather than impose that the background

*klpw3@cam.ac.uk

state be in thermal equilibrium, we work with a base state that may be actively thawing everywhere, on top of which we look for unstable growth of thawing preferential flow features. We assume that the background temperature profiles satisfy the y-independent governing equations, but rather than solving for $\bar{T}_u$ numerically, we will directly use field observations for the background vertical temperature structure (see Table S4).

On top of the horizontally uniform background state we introduce small perturbations that are periodic in the cross-slope direction with wavenumber κ (equivalent to a wavelength $\lambda = 2\pi/\kappa$) and grow exponentially at a rate $\sigma(\kappa)$ to be determined by our modeling; i.e. $T_u = \bar{T}_u(x, z, t) + \hat{T}_u(x, z)e^{i\kappa y+\sigma t}$.

We write all our variables as a background value plus small perturbation, then insert these expressions into our governing equations. After multiplying out, we retain only the terms that are linear in the perturbations, neglecting the higher order terms as much smaller. We obtain perturbed versions of all the governing equations: for mass conservation

$$\frac{d}{dx}\left(\hat{z}_{int}\frac{d\bar{p}}{dx} + \bar{z}_{int}\frac{d\hat{p}}{dx}\right) - \kappa^2 \bar{z}_{int}\hat{p} = 0, \tag{1}$$

heat production

$$\hat{Q} = 2\frac{k_0}{\mu}\frac{d\bar{p}}{dx}\frac{d\hat{p}}{dx}, \tag{2}$$

temperature diffusion in unfrozen layer

$$C_u\rho\sigma\hat{T}_u = k_u\left(\frac{\partial^2\hat{T}_u}{\partial z^2} + \frac{\partial^2\hat{T}_u}{\partial x^2} - \kappa^2\hat{T}_u\right) + \hat{Q}, \tag{3}$$

and temperature diffusion in the frozen layer

$$C_f\rho_f\sigma\hat{T}_f = k_f\left(\frac{\partial^2\hat{T}_f}{\partial z^2} + \frac{\partial^2\hat{T}_f}{\partial x^2} - \kappa^2\hat{T}_f\right). \tag{4}$$

Similarly, we find perturbed versions of all the boundary conditions: from constant pressure at the stream we obtain

$$\hat{p}(x_t) = 0, \tag{5}$$

from imposing melting temperature at the interface

$$-\left.\frac{\partial\bar{T}_u}{\partial z}\right|_{-\bar{z}_{int}}\hat{z}_{int} + \hat{T}_u(-\bar{z}_{int}) = -\left.\frac{\partial\bar{T}_f}{\partial z}\right|_{-\bar{z}_{int}}\hat{z}_{int} + \hat{T}_f(-\bar{z}_{int}) = 0, \tag{6}$$

from the melt-rate at the interface

$$\rho_w\phi L\sigma\hat{z}_{int} = k_u\left(-\left.\frac{\partial^2\bar{T}_u}{\partial z^2}\right|_{-\bar{z}_{int}}\hat{z}_{int} + \left.\frac{\partial\hat{T}_u}{\partial z}\right|_{-\bar{z}_{int}}\right) - k_f\left(-\left.\frac{\partial^2\bar{T}_f}{\partial z^2}\right|_{-\bar{z}_{int}}\hat{z}_{int} + \left.\frac{\partial\hat{T}_f}{\partial z}\right|_{-\bar{z}_{int}}\right) \tag{7}$$

$$= \bar{Q}\hat{z}_{int} + k_u\left.\frac{\partial\hat{T}_u}{\partial z}\right|_{-\bar{z}_{int}} - k_f\left.\frac{\partial\hat{T}_f}{\partial z}\right|_{-\bar{z}_{int}}, \tag{8}$$

and from heat transfer to the air

$$k_u\left.\frac{\partial\hat{T}_u}{\partial z}\right|_{z=0} = -\beta\hat{T}_u(0). \tag{9}$$

Together, these equations implicitly define the growth rate $\sigma(\kappa)$ as the value that allows the four differential equations (1-4) to be solved while respecting all the perturbed boundary conditions. We now describe the process of simplifying these differential equations based on the scales of the system so that the equations can be solved by hand, and we can extract a relatively simple and explicit expression for the growth rates.

Text S1.1 Perturbed temperature structure

We first solve for the depth-structure of the perturbed temperature profile, making the assumption that, since hillslopes are several orders of magnitude longer than the depth of the active layer, variations in temperature along the hillslope are much slower than variations with depth, and we can therefore ignore gradients in the x-direction compared to gradients in z. This reduces the diffusion equations for $\hat{T}_u$ and $\hat{T}_f$ to

$$\left(\frac{C_u\rho\sigma}{k_u} + \kappa^2\right)\hat{T}_u = \frac{d^2\hat{T}_u}{dz^2} + \frac{\hat{Q}}{k_u} \tag{10}$$

and

$$\left(\frac{C_f\rho_f\sigma}{k_f} + \kappa^2\right)\hat{T}_f = \frac{d^2\hat{T}_f}{dz^2}, \tag{11}$$

forced by the boundary conditions at the melting interface (6) and (8).

If temperature fluctuations decay deep into the frozen layer, then the solution to (11) that is at melting point at the interface, so obeying (6), is given by

$$\hat{T}_f = \frac{\partial \bar{T}_f}{\partial z}\hat{z}_{int} e^{\sqrt{\kappa^2 + C_f\rho_f\sigma/k_f}(z - \bar{z}_{int})}, \tag{12}$$

and therefore the increased heat loss into the frozen region underneath a water track is

$$\left.\frac{\partial \hat{T}_f}{\partial z}\right|_{-z_{int}} = \sqrt{\kappa^2 + \frac{C_f\rho_f\sigma}{k_f}}\frac{\partial \bar{T}_f}{\partial z}\hat{z}_{int}. \tag{13}$$

Similarly, the solution to (10) that is consistent with the expression for surface heat flux (9), while also being at melting point at the interface through (6) is

$$\hat{T}_u = \frac{\hat{Q}}{k_u\tilde{\kappa}^2}(1 - \cosh(\tilde{\kappa}z)) + \frac{\beta\sinh(\tilde{\kappa}z) - k_u\tilde{\kappa}\cosh(\tilde{\kappa}z)}{\beta\sinh(\tilde{\kappa}\bar{z}_{int}) - k_u\tilde{\kappa}\cosh(\tilde{\kappa}z_{int})}\left(\frac{\partial \bar{T}_u}{\partial z}\hat{z}_{int} - \frac{\hat{Q}}{k_u\tilde{\kappa}^2}(1 - \cosh(\tilde{\kappa}\bar{z}_{int}))\right), \tag{14}$$

where $\tilde{\kappa} = \sqrt{\kappa^2 + C_u\rho\sigma/k_u}$, and therefore the increase in heat loss through the unfrozen layer of a water track is

$$\left.\frac{\partial \hat{T}_u}{\partial z}\right|_{-z_{int}} = \frac{\hat{Q}}{k_u\tilde{\kappa}}\sinh(\tilde{\kappa}\bar{z}_{int}) + \frac{\beta\tilde{\kappa}\cosh(\tilde{\kappa}\bar{z}_{int}) + k_u\tilde{\kappa}^2\sinh(\tilde{\kappa}\bar{z}_{int})}{\beta\sinh(\tilde{\kappa}\bar{z}_{int}) - k_u\tilde{\kappa}\cosh(\tilde{\kappa}\bar{z}_{int})}\left(\frac{\partial \bar{T}_u}{\partial z}\hat{z}_{int} - \frac{\hat{Q}}{k_u\tilde{\kappa}^2}(1 - \cosh(\tilde{\kappa}\bar{z}_{int}))\right). \tag{15}$$

This accounts for heat flux from the deeper water tracks into the frozen soil that surrounds them, and the additional heat lost from the warmer water tracks into the atmosphere by conduction, only partially insulated by the snow at the surface.

In the limit of flowpaths that are much further apart than the depth of the unfrozen layer, $\tilde{\kappa}\bar{z}_{int} \ll 1$, and where heat transport across the unfrozen layer is more efficient than transfer between the air and the surface, $\beta\bar{z}_{int} \ll k_u$, equation (15) reduces to the much simpler

$$\left.\frac{\partial \hat{T}_u}{\partial z}\right|_{-z_{int}} = \frac{\hat{Q}}{k_u}\bar{z}_{int} - \left(\frac{\beta}{k_u} + \tilde{\kappa}^2\bar{z}_{int}\right)\frac{\partial \bar{T}_u}{\partial z}\hat{z}_{int}. \tag{16}$$

The first term describes changes in heating due to changes in flow speed, the second from changes in heat loss to the atmosphere, and the third from lateral heat flow from track to intertrack areas.

Inserting the perturbed heat fluxes across the thawing interface, (13) and (16), into the thaw rate (8), and using the definition of $\hat{Q}$ from (2), we find that the growth rate of perturbations to the depth of the unfrozen layer is given by

$$\rho_w\phi L\sigma\hat{z}_{int} = \bar{Q}\hat{z}_{int} + 2\frac{k_0}{\mu}\frac{d\bar{p}}{dx}\frac{d\hat{p}}{dx}\bar{z}_{int} - \beta\left.\frac{\partial \bar{T}_u}{\partial z}\right|_{-\bar{z}_{int}}\hat{z}_{int} - \sqrt{\kappa^2 + \frac{C_f\rho_f\sigma}{k_f}}k_f\left.\frac{\partial \bar{T}_f}{\partial z}\right|_{-\bar{z}_{int}}\hat{z}_{int}, \tag{17}$$

where we have dropped the term describing lateral heat transport in the unfrozen layer as it is small compared to lateral heat transport in the frozen region (again since $\tilde{\kappa}\bar{z}_{int} \ll 1$). The instability is driven by $\bar{Q}\hat{z}_{int}$, the additional heating that occurs in deeper regions of flow, which is consistent with our proposed hypothesis for water track formation. The shortest wavelengths are stabilized by lateral heat fluxes. In the following section on the along-slope depth structure of a water track, we explore how long-wavelength perturbations are stabilized through the $d\hat{p}/dx$ term. This leads to intermediate wavelength selection.

Text S1.2 Along-slope depth structure

To calculate the growth rate σ of a particular wavelength $\lambda = 2\pi/\kappa$, we must simultaneously solve the differential equations (17) and (1) for the along-slope shapes of the perturbations in active layer depth $\hat{z}_{int}$ and pressure $\hat{p}$. These equations have the form of an eigenvalue problem, that is, there is a particular value of the growth rate $\sigma(\kappa)$ such that the boundary conditions at the top and bottom of the slope are satisfied. Here our boundary conditions are the perturbations start from zero at the ridgeline, so $\hat{z}_{int}(0) = \hat{p}(0) = 0$, and that the pressure at the stream at the toeslope is fixed (hydrostatic), $\hat{p}(x_t) = 0$.

For a particular hillslope on which we had full knowledge of the background temperature and pressure fields along the full length of the slope, this eigenvalue problem could now be solved numerically, extracting the growth rates of flowpaths for this particular geometry. However, this is both impractical with our current observational record, and less useful, since by making a few further approximations we find an explicit expression for $\sigma(\kappa)$ in terms of key landscape variables (slope, ϕ, β, $\frac{\partial \bar{T}_f}{\partial z}$), gaining insight into the controls on water track spacing.

In particular, in the limit of flowpaths that are closer together than the length of the hillslope ($\kappa \gg d/dx$), the along-slope conditions change slowly, so (1) can be approximated by

$$\frac{d\bar{p}}{dx}\frac{d\hat{z}_{int}}{dx} = \kappa^2\bar{z}_{int}\hat{p}. \tag{18}$$

After differentiating (18) to find $d\hat{p}/dx$ and inserting into (17), we get the single eigenvalue equation for $\hat{z}_{int}$,

$$\frac{2\bar{Q}}{\kappa^2}\frac{d^2\hat{z}_{int}}{dx^2} = \left[\rho_w\phi L\sigma - \bar{Q} + \sqrt{\kappa^2 + \frac{C_f\rho_f\sigma}{k_f}}k_f \left.\frac{\partial \bar{T}_f}{\partial z}\right|_{-\bar{z}_{int}} + \beta \left.\frac{\partial \bar{T}_u}{\partial z}\right|_{-\bar{z}_{int}}\right]\hat{z}_{int}, \tag{19}$$

the solution to which determines $\sigma(\kappa)$, the growth rate of each possible water track spacing, and $\hat{z}_{int}(x)$, the profile of the track. However, this is still a difficult equation to solve, so we attempt to simplify the problem further.

If we ignore along-slope changes in the depth of the water track and set the left-hand side of equation (19) to 0, then the growth rate at any given point along the slope is given by

$$\rho_w\phi L\sigma_0(x) = \bar{Q} - \sqrt{\kappa^2 + \frac{C_f\rho_f\sigma}{k_f}}k_f \left.\frac{\partial \bar{T}_f}{\partial z}\right|_{-\bar{z}_{int}} - \beta \left.\frac{\partial \bar{T}_u}{\partial z}\right|_{-\bar{z}_{int}}. \tag{20}$$

The shortest wavelengths are stable ($\sigma < 0$) as we have captured the impact of efficient lateral heat diffusion out of closely spaced tracks, but the infinitely long wavelengths ($\kappa = 0$) are the most unstable. This is physically impossible, resulting from an oversimplification in the model, in particular that we have ignored the along-slope structure; a similar effect is seen in the development of subglacial channels (Warburton et al., 2024).

Instead, we consider water tracks whose depth changes as we go along the hillslope. When we account for this along-slope depth change, the largest spacings are stabilized, such that the fastest growing wavelength is at a physically realistic spacing. A key insight is that $\sigma_0(x)$ varies along the slope, since the thermal dissipation rate $\bar{Q}$, the driver of the instability, depends on the flow speed and slope angle, which increase towards the base of the hillslope. A larger growth rate further along the slope suggests deeper thaw there. To keep a deepening feature full, it must pull in water laterally from the surrounding area. With a limit on the total water flux through the system, wider tracks cannot gather enough water, so in becoming deeper they also become slower. However, since the thermal dissipation rate is proportional to flow speed, the widest tracks therefore thaw more slowly.

To quantify this further, we approximate (20) with a linear function that accounts for a gradient in the thermal dissipation rate $\bar{Q}$ along the hillslope. Using the definition of $\bar{Q}$ as

$$Q = |\boldsymbol{u} \cdot \nabla p| = \frac{k_0}{\mu}|\boldsymbol{\nabla} p|^2, \tag{21}$$

and assuming a hydrostatic pressure gradient, we find that

$$\frac{\partial \bar{Q}}{\partial x} = 2\frac{k_0}{\mu}\frac{d\bar{p}}{dx}\frac{d^2\bar{p}}{dx^2} = 2\bar{Q}\frac{d^2\bar{p}/dx^2}{d\bar{p}/dx} = 2\bar{Q}\frac{d\theta/dx}{\theta}. \tag{22}$$

If we assume a parabolic profile for the hillslope (figure S3), then $d\theta/dx = \theta/x$, and so this simplifies conveniently to

$$\left.\frac{\partial \bar{Q}}{\partial x}\right|_{x=x_t} = 2\frac{\bar{Q}(x_t)}{x_t}. \tag{23}$$

Meanwhile, we assume that the local heat transport terms in (20) do not change significantly over the length of the hillslope. A scaling argument supports this, since to satisfy the heat equation, $\bar{Q} \sim k_u T_{air}/\bar{z}_{int}^2$. Thus, again assuming track spacing is larger than active layer depth, $\tilde{\kappa}\bar{z}_{int} \ll 1$, and heat transport across the active layer is more efficient than between the atmosphere and the water track, then the $\beta \bar{z}_{int} \ll k_u$, all the remaining terms are very small compared to $k_u T_{air}/\bar{z}_{int}^2$, and therefore much smaller than $\bar{Q}$.

We can therefore write

$$\rho_w \phi L \frac{d\sigma_0}{dx} \approx \frac{2\bar{Q}}{x_t} \tag{24}$$

and use as our linear function

$$\sigma_0(x) \approx \sigma_0(x_t) + \frac{2\bar{Q}(x - x_t)}{\rho_w \phi L x_t}. \tag{25}$$

Inserting (25) into the eigenvalue equation (19), we end up with

$$\frac{2\bar{Q}(x_t)}{\rho_w \phi L \kappa^2} \frac{d^2 \hat{z}_{int}}{dx^2} = \left[\sigma(\kappa) - \sigma_0(x_t) - \frac{2\bar{Q}(x - x_t)}{\rho_w \phi L x_t} \right] \hat{z}_{int}, \tag{26}$$

which now is simple enough to solve analytically for $\sigma(\kappa)$, while still capturing the mechanisms leading to wavelength selection. Similarly to the case of subglacial channels (Warburton et al., 2024), we have obtained a rescaled version of Airy's equation, for which exact solutions exist, such that a direct extraction of growth rate can be obtained without having to solve (19) numerically.

In particular, defining rescaled variables

$$\sigma_0(x_t) - \sigma(\kappa) = S \frac{2\bar{Q}}{\rho_w \phi L} \left(\frac{1}{\kappa x_t} \right)^{2/3}, \quad x_t - x = \left(\frac{x_t}{\kappa^2} \right)^{1/3} X, \tag{27}$$

our governing equation (26) simplifies to

$$\frac{\partial^2 \hat{z}_{int}}{\partial X^2} = (X - S)\, \hat{z}_{int}, \tag{28}$$

exactly Airy's equation with a shifted coordinate system, with the rescaled growth rate S setting the shift. Thus, the shape of $\hat{z}_{int}(x)$ is an Airy function, $Ai(X - S)$. We find S, and hence $\sigma(\kappa)$, by applying the pressure boundary condition $\hat{p}(x_t) = d\hat{z}_{int}/dx(0) = 0$, and so S must be a value where the Airy function has zero gradient. In particular, the largest growth rate will be associated with the smallest possible value of S, which is $S = 1.0187\ldots$.

Text S1.3 Wavelength selection

Reassembling $\sigma(\kappa)$, we find that the growth rate of flowpaths on a hillslope at a wavenumber κ is given by

$$\rho_w \phi L \sigma = \bar{Q} - \beta \frac{\partial \bar{T}_u}{\partial z} - \sqrt{\kappa^2 + \frac{C_f \rho_f \sigma}{k_f}}\, k_f \frac{\partial \bar{T}_f}{\partial z} - \frac{2.0374\, \bar{Q}}{(\kappa x_t)^{2/3}}, \tag{29}$$

which is stable at both the shortest wavelengths (large κ) due to lateral diffusion of heat, and the longest wavelengths (small κ) due to the pressure gradients induced by limits on water availability in the system. We therefore can expected wavelength selection at an intermediate value of κ.

Differentiating with respect to κ to find the most unstable wavenumber, we have $d\sigma/d\kappa = 0$ when

$$\frac{\kappa}{\sqrt{\kappa^2 + C_f \rho_f \sigma / k_f}} k_f \left. \frac{\partial \bar{T}_f}{\partial z} \right|_{-\bar{z}_{int}} = \frac{2.0374\, \bar{Q}}{(\kappa^5 x_t^2)^{1/3}} \tag{30}$$

where all quantities are evaluated at x_t. Note that this expression does still depend on σ, so would have to be evaluated numerically for complete generality. However, if the maximum growth rate occurs when neither lateral heat transport nor pressure gradients are large, then

$$\sigma_{max} \approx \frac{1}{\rho_w \phi L} \left(\bar{Q} - \beta \left. \frac{\partial \bar{T}_u}{\partial z} \right|_{-\bar{z}_{int}} \right), \tag{31}$$

the sign of which depends on whether deeper thaw is unstable due to the increased heat production in regions of deeper flow, or stable due to being at increased depth, such that there is less heat coming from the surface. In regions where $\sigma_{max} > 0$, melt-driven channelization is possible, and the most unstable wavenumber is approximately given by the root of

$$\frac{\kappa^{8/3}}{\sqrt{\kappa^2 + C_f \rho_f \left(\bar{Q} - \beta \frac{\partial \bar{T}_u}{\partial z} \right) / k_f \rho_w \phi L}} = \frac{2.0374\, \bar{Q}}{k_f \frac{\partial \bar{T}_f}{\partial z} x_t^{2/3}} \tag{32}$$

where all quantities are evaluated at $x = x_t$, and the temperature gradients are evaluated at the base of the unfrozen layer. The associated wavelength is $\lambda = 2\pi/\kappa$.

A technical consideration when interpreting the output of our model is that the modeling assumptions break down at very small and very large wavelengths. Our solution to the thermal model relies on the simplification that the inter-track distance is greater than the depth of the active layer. In the high flow speed, high slope angle regime that appears to predict closely spaced tracks, we would have to numerically solve for the temperature. However, observations consistently show tracks spaced wider than the active layer depth, and there are few places in the literature reporting water tracks on slopes above 20°. At slopes greater than 20°, advection and diffusion of sediment might start to control flowpaths, and true fluvial channels or rills may form.

Figures S1 to S5

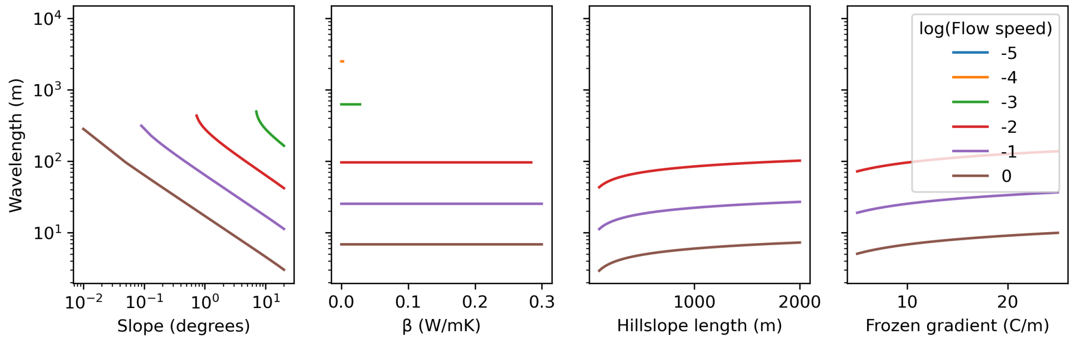

Figure S1: Sensitivity of the fastest growing wavelength to control parameters, across a range of flow speeds. Wavelength is not shown when the associated largest growth rate (figure S2) is negative, and thus are not shown for the smallest flow speeds except at very high slope angles or high degrees of insulation (low β). Default values are $x_t = 1600$, $\theta = 5°$, $\phi = 0.9$, $\frac{\partial \bar{T}_f}{\partial z} = 10$, $\beta = 0.04$.

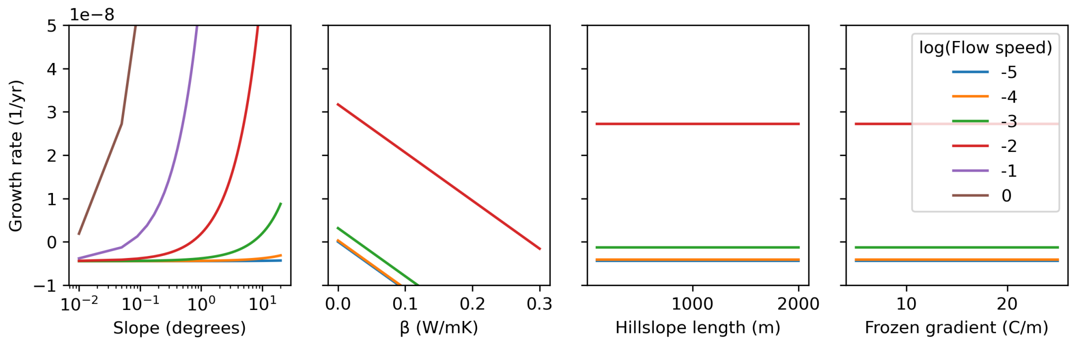

Figure S2: Sensitivity of the maximum growth rate to control parameters. Default values are $x_t = 1600$, $\theta = 5°$, $\phi = 0.9$, $\frac{\partial \bar{T}_f}{\partial z} = 10$, $\beta = 0.04$. Growth rate depends on a balance between dissipative heat flux (a function of slope and flow rate) and conductive heat loss (a function of β and $\partial \bar{T}_u / \partial z$) only.

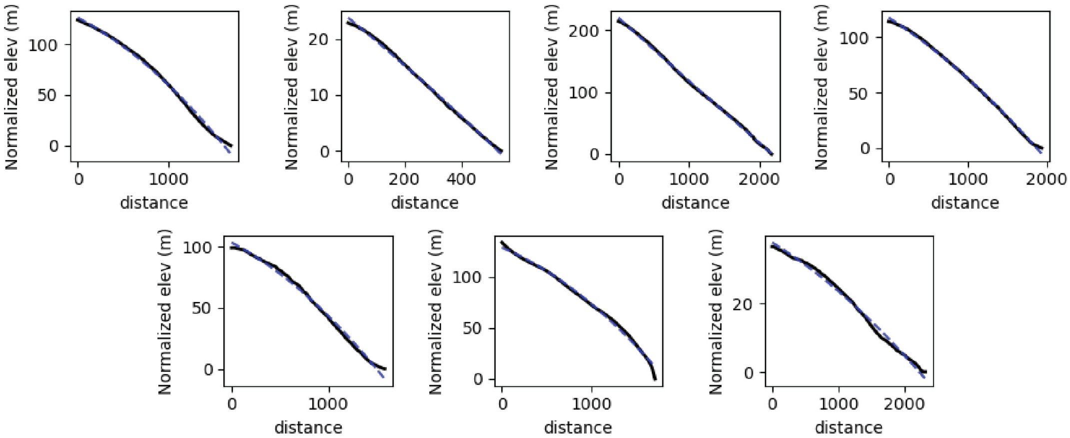

Figure S3: Topographic profiles of hillslopes with water tracks, and quadratic fits to their shapes.

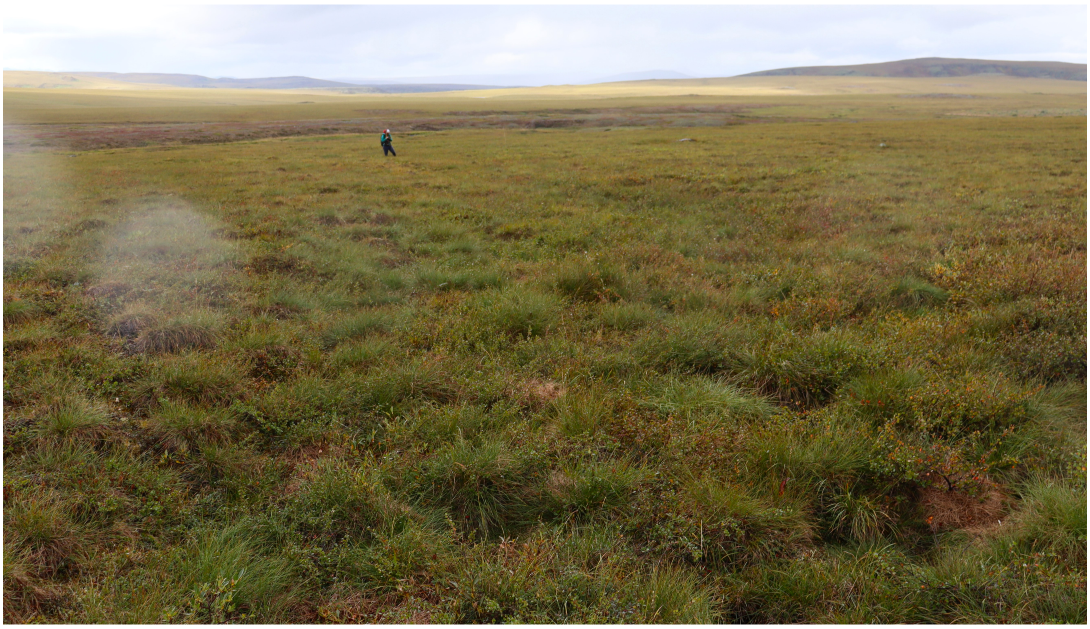

Figure S4: Field photo of the new water track pictured in Figure 4 in August 2024. Tussocks in the center and foreground are slightly greener and uneven and exhibit evidence of subsidence of the surrounding ground compared to the tussocks on the edges of the photo.

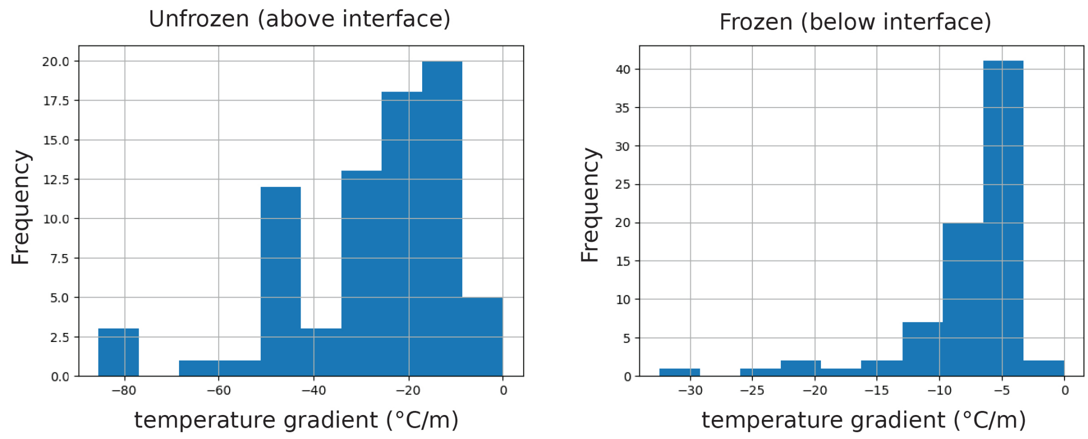

Figure S5: Histograms of temperature gradients in the unfrozen and frozen soil at the top of the permafrost table at Water Track 6 from 2012-2014 (Godsey, 2020). Gradients are computed by resampling thermal data daily, identifying the depth at which temperature switches from positive to negative, and then computing the gradient above and below that switch point.

Tables S1 to S4

Variable	Definition
$\boldsymbol{u}$	Darcy flux (m/s)
p	water pressure (Pa)
$\boldsymbol{q}$	water flux through unfrozen layer (m^2/s)
z_{int}	depth of the permafrost table (m)
Q	dissipative heating per unit volume (W/m^3)
T_u	temperature of unfrozen layer (K)
T_f	temperature of frozen layer (K)

Table S1: Variables used in the model: symbol, definition and units

Variable	Definition	Value
ρ_w	density, water (kg/m^3)	1000
ρ_s	density, sediment (kg/m^3)	2600
ρ_i	density, ice (kg/m^3)	900
C_w	specific heat capacity, water (J/K kg)	4184
C_s	specific heat capacity, sediment (J/K kg)	700
C_i	specific heat capacity, ice (J/K kg)	2050
k_w	thermal conductivity, water (W/m K)	0.598
k_s	thermal conductivity, sediment (W/m K)	1.460
k_i	thermal conductivity, ice (W/m K)	2.220
g	gravitational constant (m/s^2)	9.8
μ	viscosity, water (kg/ms)	8.9 x 10^{-4}
L	latent heat of melting (J/kg)	3.34 x 10^5

Table S2: Physical constants used in the model: symbol, definition, units, and value.

Variable	Name	Value
C_f	specific heat, frozen layer (J/K kg)	1915
C_u	specific heat, unfrozen layer (J/K kg)	3835.6
k_f	thermal conductivity, frozen layer (W/m K)	2.728
k_u	thermal conductivity, unfrozen layer (W/m K)	1.2682

Table S3: Derived thermal constants for the soil, based on porosity of 0.9

Variable	Name	June	August
Q_{wt}	discharge, water track (m^3/day)	955.6	21.6
d_{wt}	thaw depth, water track (m)	0.10	0.70
K_{wt}	bulk flow rate, water track (m/day)	1194.5	3.86
w_{wt}	width, water track (m)	8	
x_t	hillslope length (m)	1600	
θ	slope (°)	4.8	
β	insulation parameter (W/m^2 K)	0.04	
$\partial T_u/\partial z\|_{-\bar{z}_{int}}$	thermal gradient in the frozen layer at the interface (C/m)	[5, 25]	

Table S4: Parameter values measured at Toolik, representing peak June flows with minimal thaw and average August flows with maximum thaw (Evans et al., 2020) and field measurements, used in Figure 3 of the main paper.

Caption for Video S1

Flow through the vegetation mat of a water track following a rain event, Toolik, August 2024. Leaves and grasses transported by the flow indicate a speed of approximately 0.25m/s.

References

Sarah G. Evans, Sarah E. Godsey, Caitlin R. Rushlow, and Clifford Voss. Water tracks enhance water flow above permafrost in upland arctic alaska hillslopes. *Journal of Geophysical Research: Earth Surface*, 125(2), 2020. ISSN 2169-9003, 2169-9011. doi: 10.1029/2019JF005256. URL https://onlinelibrary.wiley.com/doi/10.1029/2019JF005256.

Sarah Godsey. Soil temperatures at water track sites. Arctic Data Center. https://arcticdata.io/catalog/view/8fa6477d-f846-4daa-b053-c799a8b11825, 2020.

K. L. P. Warburton, C. R. Meyer, and A. N. Sommers. Predicting the onset of subglacial drainage channels. *Journal of Geophysical Research: Earth Surface*, 129(12):e2024JF007758, 2024. doi: https://doi.org/10.1029/2024JF007758. URL https://agupubs.onlinelibrary.wiley.com/doi/abs/10.1029/2024JF007758. e2024JF007758 2024JF007758.